◆ ANNUAL ISSUE

EARLY CAREER SCHOLARS IN MATERIALS SCIENCE 2022

Growth of nanoporous high-entropy oxide thin films by pulsed laser deposition

Huiming Guo[1], Xin Wang[1], Alexander D. Dupuy[1], Julie M. Schoenung[1],
William J. Bowman[1,2,a]

[1] Department of Materials Science and Engineering, University of California, Irvine, Irvine, USA
[2] Irvine Materials Research Institute, University of California, Irvine, Irvine, USA
[a] Address all correspondence to this author. e-mail: will.bowman@uci.edu

High-entropy oxides (HEO) with entropic stabilization and compositional flexibility have great potential application in batteries and catalysis. In this work, HEO thin films were synthesized by pulsed laser deposition (PLD) from a rock-salt $(Co_{0.2}Ni_{0.2}Cu_{0.2}Mg_{0.2}Zn_{0.2})O$ ceramic target. The films exhibited the target's crystal structure, were chemically homogeneous, and possessed a three-dimensional (3D) island morphology with connected randomly shaped nanopores. The effects of varying PLD laser fluence on crystal structure and morphology were explored systematically. Increasing fluence facilitates film crystallization at low substrate temperature (300 °C) and increases film thickness (60–140 nm). The lateral size of columnar grains, islands (19 nm to 35 nm in average size), and nanopores (9.3 nm to 20 nm in average size) increased with increasing fluence (3.4 to 7.0 J/cm^2), explained by increased kinetic energy of adatoms and competition between deposition and diffusion. Additionally, increasing fluence reduces the number of undesirable droplets observed on the film surface. The nanoporous HEO films can potentially serve as electrochemical reaction interfaces with tunable surface area and excellent phase stability.

William J. Bowman

William J. Bowman joined the Department of Materials Science and Engineering at University of California, Irvine in 2019. He received a B.S.E. in Materials Science and Engineering from Arizona State University in 2012 and a Ph.D. in same department in 2016. During graduate school, he was a visiting Ph.D. student at ETH Zürich in the Department of Materials. After graduate school, he was a Postdoctoral Associate at MIT in the Department of Nuclear Science and Engineering. Bowman's research focuses on understanding and developing oxide ceramics and nanomaterials for electrochemical energy conversion and storage, as well as carbon dioxide capture. The Bowman Lab performs materials synthesis, testing, and multiscale characterization primarily using advanced electron microscopy. His research has been financially supported by The National Science Foundation, The Research Corporation for Science Advancement, The American Chemical Society, The Microscopy Society of America, and the UCI School of Engineering. He has received the NSF CAREER award, the NSF Graduate Research Fellowship, the Swiss Government Excellence Scholarship, the NSF Graduate Research Opportunities Worldwide Award, the Microscopy Society of America Presidential Scholar Award, and the Arizona State University Doctoral Enrichment Fellowship. He is a member of the Microscopy Society of America, the Microanalysis Society of America, the Materials Research Society, TMS, and the National Society of Black Engineers.

Introduction

Oxide ceramics are widely used because they exhibit a wide range of properties originating from their diverse and tunable structure, such as crystallography, microstructure, and electron density. As for oxide structure design, in addition to chemical doping where minor additional elements/solutes dissolve in the matrix, engineering the configurational entropy has been discovered recently for designing complex multicomponent oxides with expansive composition spaces and the potential for tunable system disorder, as entropy can dominate the Gibbs free energy at elevated temperature ($\Delta G = \Delta H - T\Delta S$) [1]. These complex concentrated oxides are often called high-entropy oxides (HEOs) or entropy-stabilized oxides (ESOs) and they consist of five or more oxide components with equimolar or near-equimolar concentrations that can be incorporated into a single solid solution phase wherein cations randomly occupy a cation sublattice [2, 3]. HEOs also have tolerance for cation multivalency and ionic vacancies, so lattice distortion, oxygen off-stoichiometry and even aliovalent cation additions can be tuned for property design [4]. Some HEOs have suitably served as anode or cathode materials in Li/Na ion batteries with long cycling stability and high-capacity retention due to phase stability and high alkali ionic conductivity, while HEO-supported noble metal catalyst systems exhibit great catalytic efficiency in CO oxidation and

CO_2 reduction owing to high temperature stability and flexible cation availability [5]. In this article, a model rock-salt HEO $(Co_{0.2}Ni_{0.2}Cu_{0.2}Mg_{0.2}Zn_{0.2})O$ served as target materials for fabrication of HEO thin films with tunable nanoscale porosity and morphology.

Pulsed-laser deposition (PLD) is a physical vapor deposition technique capable of growing multicomponent oxide thin films with controllable crystallinity, microstructure, and nanoscale morphology, and is thereby widely used in structure–property relation research of electrochemical, dielectric, ferroelectric, magnetic, and high-temperature superconducting fields [6–10]. KrF excimer lasers with 248 nm wavelength and 20–35 ns pulse duration are the most commonly used laser source, while solid-state lasers, such as frequency quadrupled Nd:YAG with a 266 nm wavelength and 5–10 ns pulse duration, have been gradually becoming more popular recently due to nontoxicity and small volume for convenient transport and placement [11]. During growth, high-powered laser pulses enter a vacuum chamber and hit a condensed material (target), leading to a rapid temperature increase beyond the evaporation temperature in a small portion of the target surface [12]. During the laser-target interaction, material is removed from the target surface in the form of a plasma plume containing atomic and ionic components (in addition to photon absorption by the target). The plume expands
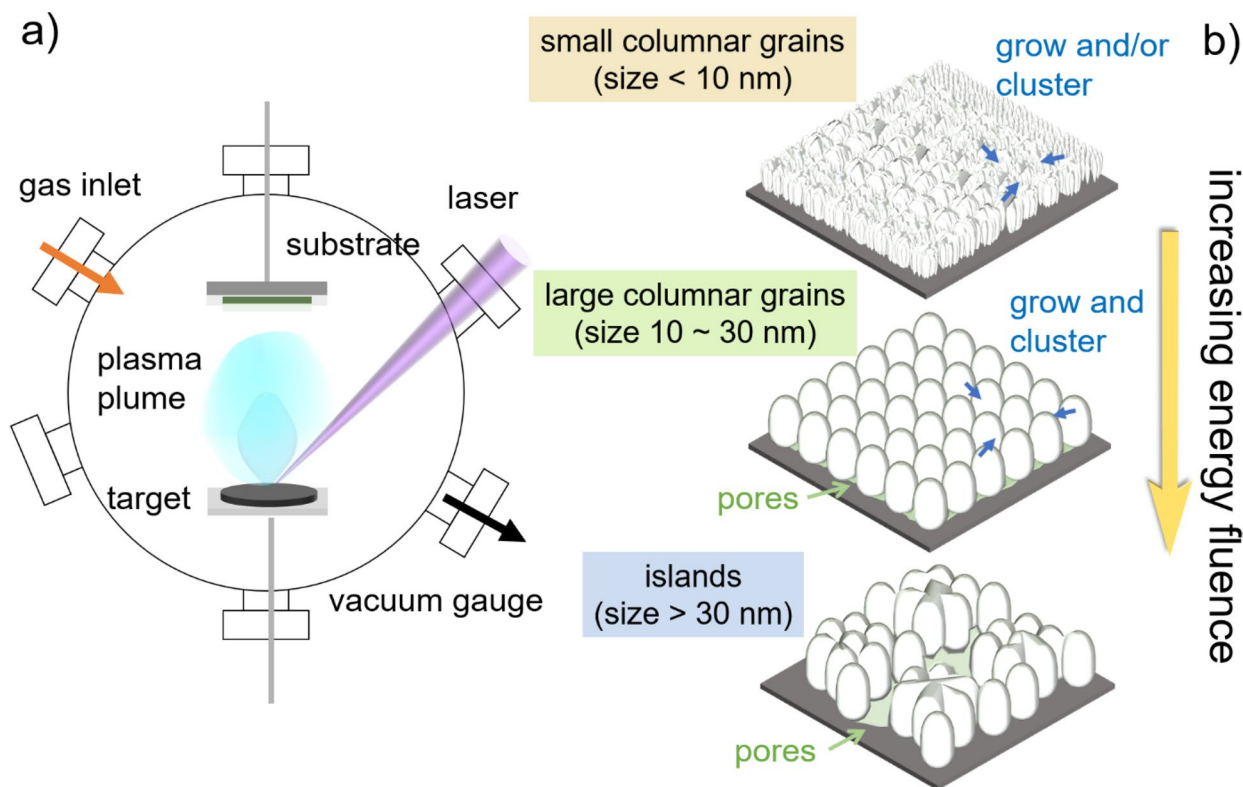

Figure 1: Schematic of (a) principle of pulsed laser deposition (PLD) and (b) effect of increasing energy fluence on 3D island structure of prepared thin films.

rapidly into the vacuum and then recondenses on the surface of a nearby substrate [13] (Fig. 1a). Congruent evaporation in PLD helps achieve highly stoichiometric and high-quality film deposition, which is beneficial for epitaxial, multilayer, polycrystalline, and even amorphous film fabrication [12]. Due to the high plasma plume energy, PLD growth is possible over a range of chamber pressures, background gas compositions, and substrate temperatures; the latter is beneficial if one aims to grow temperature-sensitive materials which, as is the case for the HEO target used here, are known to form secondary phases between 450 and 850 °C [14]. PLD has great advantages for film fabrication of these entropy-stabilized compounds and even ones with metastable states [4]. Laser plasma has a much higher $T\Delta S$ term than bulk annealing, so it facilitates the formation of the high-entropy solid solution phase [15]. When adatoms arrive at the substrate surface, they will quench rapidly to freeze the single phase. Additionally, as a high energy method, kinetic energy of adatoms can be controlled in PLD for producing structures far from thermodynamic equilibrium. The existence of lattice distortion and cation multivalency endows HEOs with many nonequilibrium phases and PLD provides a flexible and effective platform for research of these phases [4, 16].

Normally, the mismatch between substrate lattice and target structure facilitates thin film growth by the Volmer-Weber growth mode, which forms three-dimensional (3D) island structures instead of layer-by-layer epitaxial growth on the substrate [16, 17]. There exists an additional energy barrier to adatom diffusion at descending step edges of existing columnar grains, named the Ehrlich–Schwoebel (ES) barrier, so adatoms may preferentially nucleate on the top of existing columnar grains (and islands), resulting in peak/pyramid-shaped columnar grain tops [18, 19]. Whether adatoms can overcome the ES barrier relates to the competition between deposition rates and diffusion rates. Adatoms with sufficient mobility can cross the ES barrier and will form boundaries between columnar grains. Yet, adatoms with low mobility are not able to overcome the ES barrier so holes or gaps will form between each columnar grain and the fabricated films are nanoporous [20]. These nanoporous films with large surface areas have great potential applications in catalysts, sensors, and electrodes. For example, S. Shin, et al. deposited tree-like nanoporous WO_3 thin films by PLD and used them as the photoanode in photoelectrochemical water oxidation. They showed that large surface area, a high number of active sites, and the partially preferred alignment of individual WO_3 nanocrystals greatly increased charge transfer efficiency and photocurrent density [21]. G. Atanasova et al. fabricated highly porous noble metal–metal oxide (Au–ZnO) nanocomposites by PLD as gas sensors and the nanoporous composites exhibited high sensitivity to NH_3 vapor at room temperature [22]. A. Infortuna et al. fabricated nanoporous nickel oxide–gadolinia-doped ceria (NiO–$Ce_{0.8}Gd_{0.2}O_{1.9-x}$) thin films
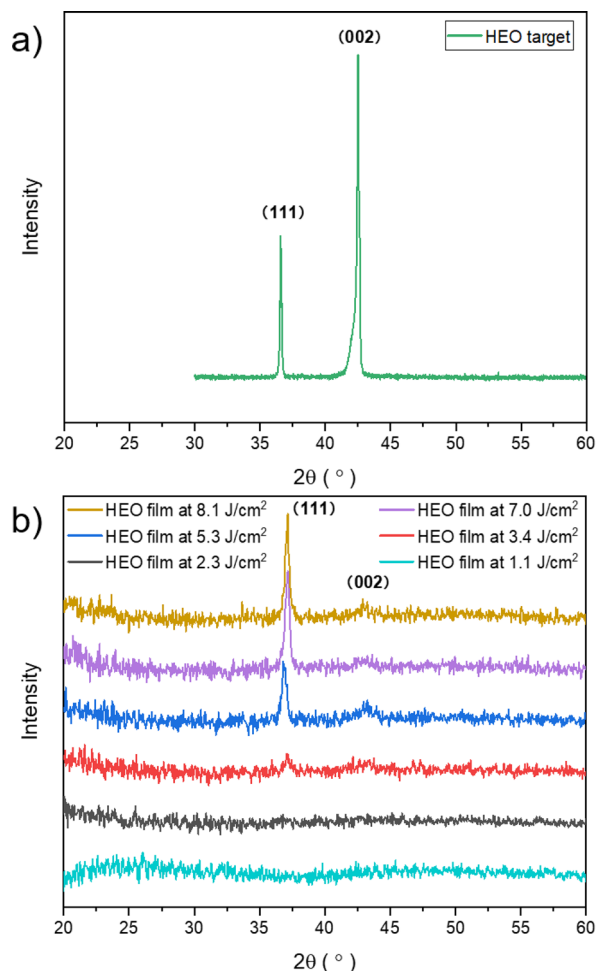
Figure 2: XRD patterns of HEO target and thin films prepared by PLD at different energy fluence. (a) XRD pattern of rock-salt HEO target in θ-2θ geometry; (b) XRD patterns of prepared HEO thin films deposited at 1.1 J/cm² to 8.1 J/cm² in θ-2θ geometry.

by PLD and then reduced the NiO phase in a H_2/N_2 atmosphere to create a stable three-phase (metallic Ni, ceramic, and pores), 3D interconnected microstructure for the anode of solid oxide fuel cell (SOFC) [23]. Hence, it is worth determining deposition conditions for controllable nanoporous structure growth in other promising complex ceramic oxides for electrochemical applications.

High supersaturation of the plasma/vapor leads to a high nucleation rate far from thermodynamic equilibrium, so film growth in PLD is governed by kinetic effects, like adatom mobility on the substrate surface and experimental conditions including energy fluence, substrate temperature, ambient pressure, laser repetition rate, and substrate–target distance [24]. Competition between surface diffusion and nucleation and growth of seeds determines thin film morphology, such as 2D layers or 3D islands [25]. The effective diffusion coefficient of colliding atoms relies on the kinetic energy of the ablated plasma/vapor [26].

High kinetic energy increases the surface mobility of arriving atoms (adatoms) and particles, facilitates gas-phase reactivity with any inlet/background gas in the chamber, enhances surface reactions with the substrate, and can reduce the requisite deposition temperature [12]. Among PLD experimental parameters, energy fluence (controlled here by laser voltage) determines the kinetic energy of ablated atoms/particles and is thus highly related to thin film structure [16]. In this research, a series of HEO thin films were prepared by PLD at different energy fluence values using a Nd:YAG solid-state laser to explore the effect of energy fluence on film crystallization, island structure, and nanoporous morphology, which lays a foundation for future design of controllable nanoporous complex oxide films.

Results and discussion

The XRD pattern for the HEO target confirmed the rock-salt structure without any secondary phases (Fig. 2a and Fig SI-1). A relatively low substrate temperature (300 °C) was set to avoid secondary phase formation in the film, which is known to form in the bulk ceramic of this HEO [14]. The peak positions of the films (Fig. 2b) matched with the target (Fig. 2a), showing that both have the same crystal structure and there are no secondary phases in the deposited HEO thin films. XRD data from θ-2θ geometry showed both (111) and (002) peaks (Fig. 2b), indicating that the fabricated HEO films are polycrystalline. Comparing the peak intensity of the films deposited at 5.3 J/cm^2, 7.0 J/cm^2, and 8.1 J/cm^2 (Fig. 2b) and that of the target (Fig. 2a), it was shown that the intensity ratio of (111) to (002) of the film is much higher than that in the bulk where the intensity of (111) peak is far weaker than that of (002) peak, thereby highlighting the preferred [111] orientation of the prepared films. V. Jacobson, et al. deposited polycrystalline rock-salt HEO (($Co_{0.2}Ni_{0.2}Cu_{0.2}Mg_{0.2}Zn_{0.2}$)O) films on different substrates and at different environment conditions by PLD and their fabricated polycrystalline films also showed preferred orientation [15]. Hence, preferred orientation is a characteristic of HEO polycrystalline films but it is highly related to substrate types, temperature, and pressure.

At very low energy fluence of 1.1 J/cm^2, the HEO film was amorphous without any diffraction peaks, but with an amorphous peak at 2θ between 20 and 30°. With the increase of energy fluence from 2.3 to 8.1 J/cm^2, the amorphous peak disappeared, and the diffraction peaks gradually became intense, indicating that the films gradually crystallized. Higher fluence results in higher kinetic energy of adatoms, which accelerates crystallite nucleation and growth. In theory, increasing both the substrate temperature and the energy fluence can increase the energy available to adatoms needed to accelerate the diffusion and crystallization processes. In the case of this HEO, which is known to form secondary phases at intermediate temperatures

of ~ 450 °C if grain size is at the nanometer scale [14], it is a good strategy to use a high laser fluence to deposit adatoms on a substrate with low temperature.

To investigate the texture developed in the prepared HEO thin films, orientation mapping was performed by TEM precession electron diffraction (TEM PED). Figure 3a shows an inverse pole figure (IPF) color map of the HEO thin film with the silicon substrate at the bottom. The grains are color coded according to the inset IPF color key along the deposition direction (i.e., the vertical direction in the map). The HEO film fabricated at 5.3 J/cm^2 showed nano-sized columnar grains. Figure 3b and c shows calculated pole figures for the rock-salt HEO and Si phases, respectively. It is apparent that the deposition direction is parallel to the [001] direction of Si. Moreover, there is a relatively weak texture for the HEO thin film with the peak intensity being 5.4 MUD (multiples of uniform distribution). By comparing the pole figures for HEO and Si, the orientation relationships between the thin film and the substrate are [111]HEO//[001] Si and [110]HEO//[110]Si. The TEM PED results matched the XRD data and characterized preferred [111] orientation and polycrystalline structure of the fabricated HEO film.

Thin film surface morphology changed greatly at various energy fluence (Fig. 4). At 1.1 J/cm^2 and 2.3 J/cm^2 (Fig. 4a, b), the films are more continuous in the planar direction without an obvious 3D island structure but with some minor gaps that are probably from the early stages of island formation and/or shrinkage during cooling. Considering the XRD data (Fig. 2a), these low energy fluences are not sufficient to nucleate and grow crystalline grains. With an increase of energy fluence from 3.4 to 7.0 J/cm^2, the average size of columnar grains and islands change from 19 to 35 nm (Fig. 4g–i). The columnar grains gradually adopt a triangle shaped morphology with the rise of energy fluence from 3.4 (Fig. 4c) to 5.3 J/cm^2 (Fig. 4d), suggesting that more columnar grains grow and/or cluster together along extended (111) terraces with triangle symmetry [27].

It is assumed that adatoms crystalize to form individual small columnar grains (size < 10 nm). These columnar grains grow and/or cluster together to form large columnar grains (size 10–30 nm) with a visible 3D island structure separated by narrow pores. Interestingly, with the further increase of energy fluence (> 5.3 J/cm^2), independent large columnar grains cluster together to form islands (size > 30 nm) with large distances between adjacent islands, i.e., porosity (Fig. 4e, f). As mentioned in the introduction, adatoms with high kinetic energy are more likely to overcome the ES barrier for diffusing and hopping at the edges. Hence, films deposited at higher energy fluence tend to have larger columnar grains and islands.

Columnar grains and islands are compact and uniform in films deposited at 3.4 J/cm^2 (Fig. 4c) and 5.3 J/cm^2 (Fig. 4d), while they look disconnected and tortuous in films deposited at 7.0 J/cm^2 (Fig. 4e) and 8.1 J/cm^2 (Fig. 4f). The circled areas
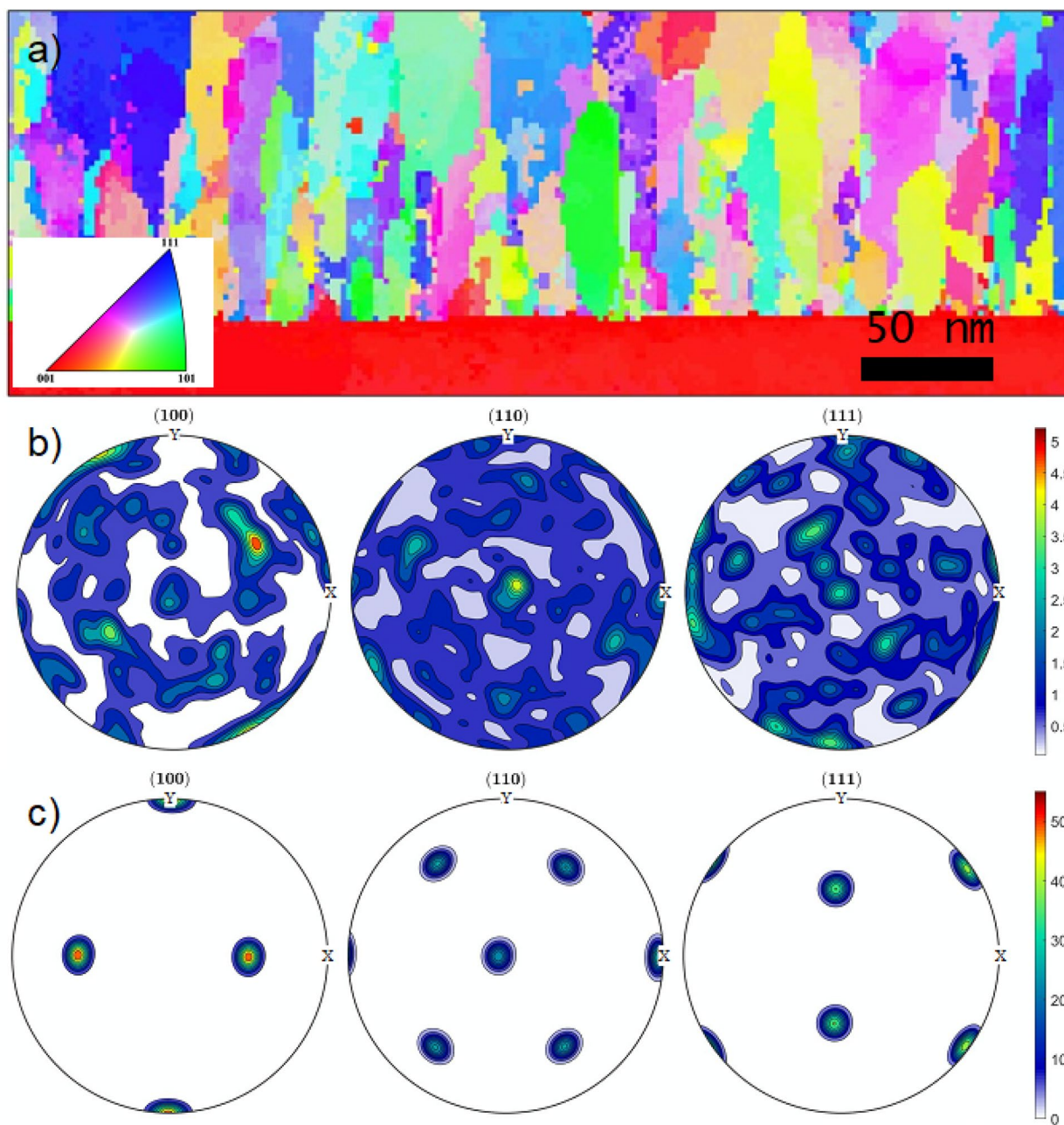
Figure 3: Orientation mapping of the fabricated HEO thin film deposited at 5.3 J/cm^2 with PED: (a) inverse pole figure (IPF) colored map relative to the deposition (vertical) direction; (b), (c) the pole figures for HEO and the Si substrate, respectively, which indicate a texture in the HEO thin film with [111] HEO//[001]Si and [110]HEO//[110]Si.

in Fig. 4e,f highlight the process of island formation (Fig. 1b), where the columnar grains gradually became rounded, neighboring islands combined, and the nanopores became wider and more interconnected in the lateral directions with random shape throughout the film. There are two factors leading to the phenomena: deposition-driven island–island impingement and surface-diffusion-driven island–island coalesce [28]. Firstly, during the deposition, columnar grains will continue to grow, touch, and impinge with their neighbors to form islands [16].

Additionally, columnar grains begin to coalesce driven by capillary effect for a more thermodynamical equilibrium state, where atoms can exchange between columnar grains [16, 29]. The clusters of coalescing columnar grains will form islands and leave large gaps/holes inside the film. The average nanopore size of the HEO films deposited at 3.4 J/cm^2, 5.3 J/cm^2, 7.0 J/cm^2, and 8.1 J/cm^2 is 9.3 nm, 17 nm, 20 nm, and 25 nm, respectively (Fig SI-3). The largest pore size in the HEO film deposited at 8.1 J/cm^2 is 80 nm, much larger than that in the film deposited at 3.4 J/cm^2,
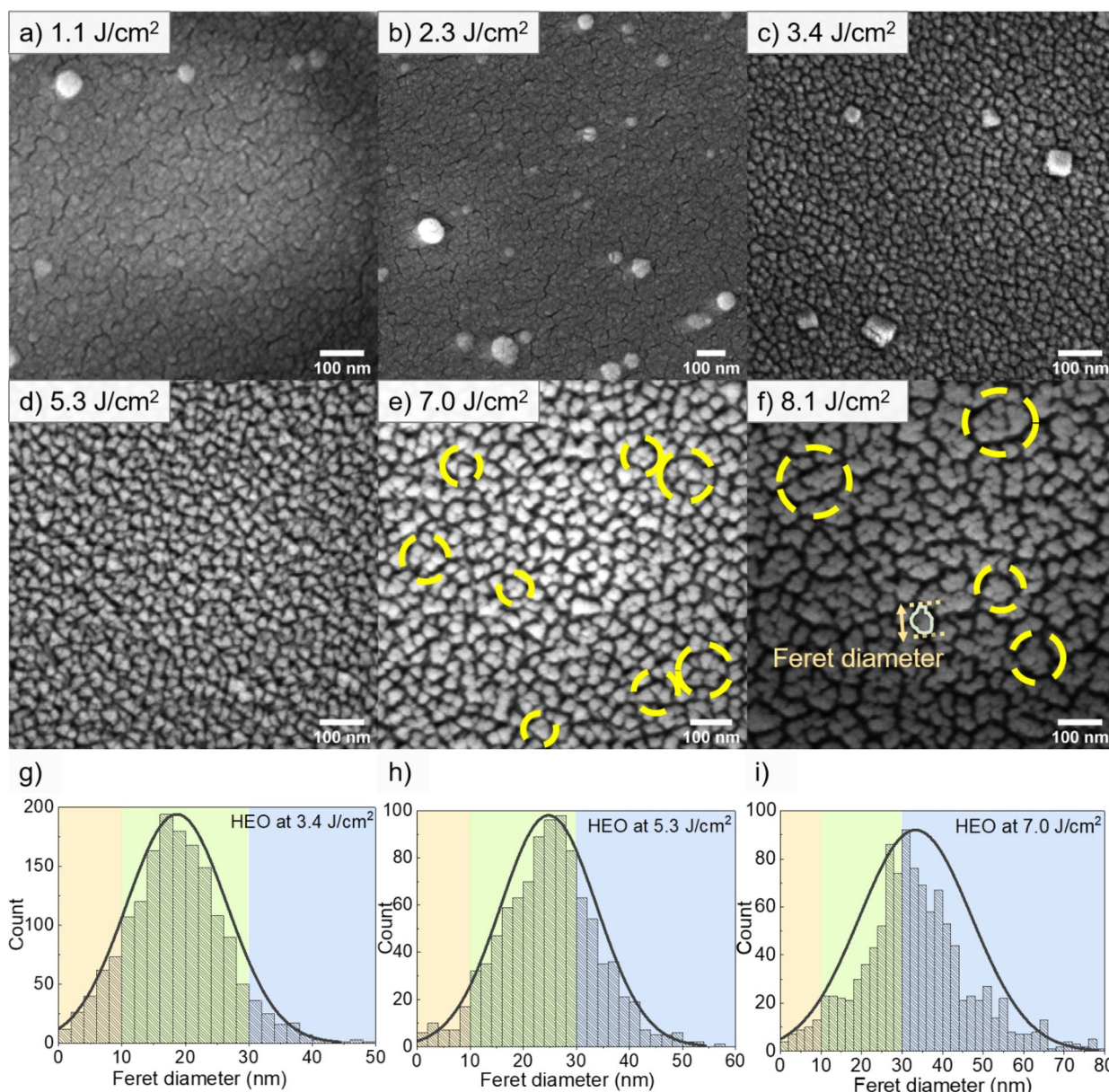
Figure 4: SEM images of the top view of the HEO thin films prepared by PLD at different energy fluence: (a) 1.1 J/cm^2; (b) 2.3 J/cm^2; (c) 3.4 J/cm^2; (d) 5.3 J/cm^2; (e) 7.0 J/cm^2; (f) 8.1 J/cm^2; Circled area showed columnar grains tend to grow and cluster together to form islands at high energy fluence; (g)-(i) the size distribution of columnar grains and islands at 3.4 J/cm^2, 5.3 J/cm^2 and 7.0 J/cm^2; the size of columnar grains and islands were described with Feret diameter as shown in (f); the yellow, green, and blue areas in (g)–(i) represent the size range of small columnar grains (< 10 nm), large columnar grains (10–30 nm), and islands (> 30 nm), respectively.

which is only 23 nm. The fraction of islands and the gap width in the film gradually increased with the increase of energy fluence. Therefore, energy fluence can be applied to control the size of columnar grains, islands, and the width of nanopores.

The 3D island structures and nanopores are visible by cross-section SEM (Fig. 5) and TEM (Fig. 6). Like the top view (Fig. 4b), the film deposited at 2.3 J/cm^2 showed minor island structure—composed of amorphous and partially crystalline phases—separated by narrow gaps which likely result from

the early stage of island formation or shrinkage during cooling (Fig. 5a). At higher energy fluence (> 2.3 J/cm^2; Fig. 5b–e), films are more crystalline and exhibit a distinctive 3D island structure made up of columnar grains, islands, and nanopores. The film thickness increased from 60 to 140 nm with increasing energy fluence from 1.1 to 5.8 J/cm^2 (Fig. 5f), which corresponded to a brighter and larger plasma plume (Fig SI-1). The thickness declined at 7.0 J/cm^2, indicating that excessive fluence leads to rebounding of adatoms or sputtering of the film.
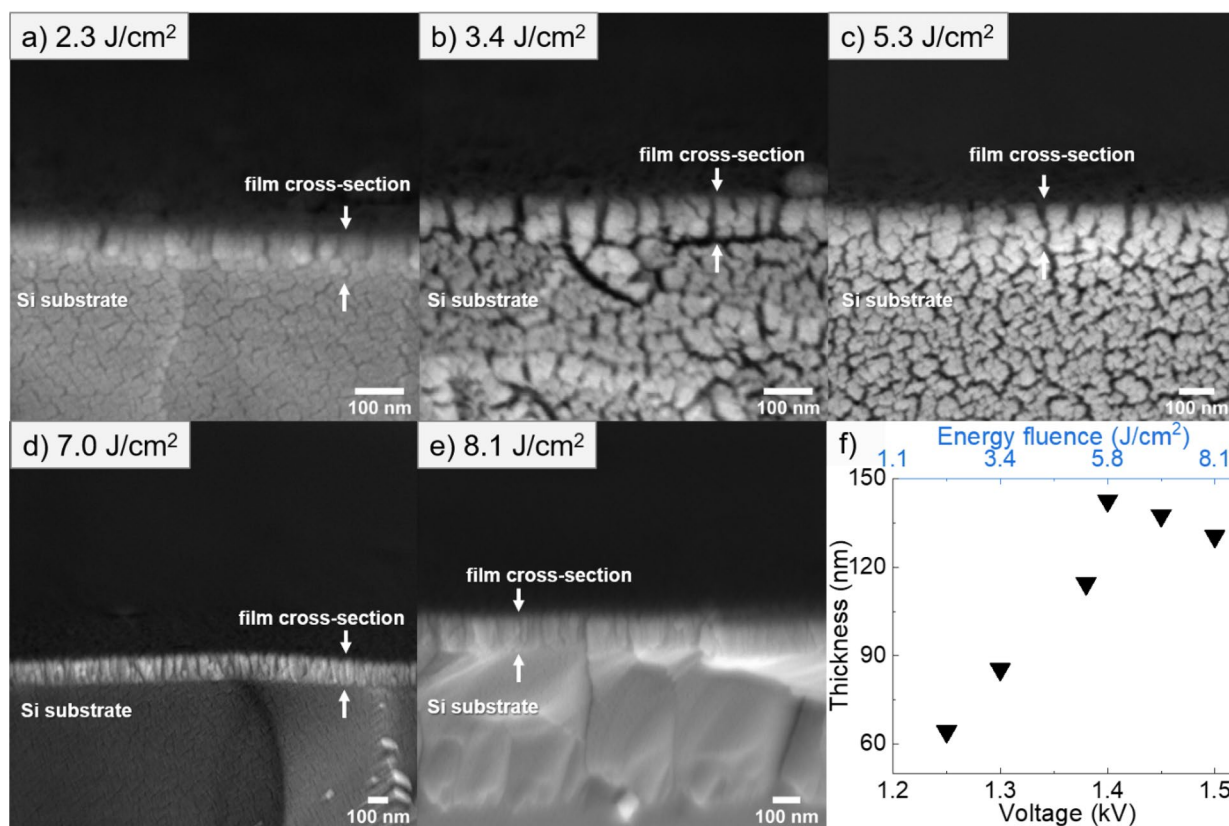
Figure 5: SEM images of cross-section view of HEO thin films prepared at different energy fluence: (a) 2.3 J/cm²; (b) 3.4 J/cm²; (c) 5.3 J/cm²; (d) 7.0 J/cm²; (e) 8.1 J/cm²; (f) film thickness as a function of voltage and energy fluence.

The columnar grains and nanopores of the HEO film deposited at 5.3 J/cm² were observed by bright-field transmission electron microscopy (BFTEM) and high-resolution transmission electron microscopy (HRTEM) (Fig. 6a, b). Consistent with the TEM PED results (Fig. 3), columnar grains in TEM images showed diffraction contrast, lattice fringes, and rough or jagged faceted shapes on the grain sides and top. The selected area electron diffraction (SAED) pattern acquired in the film (inset of Fig. 6b) showed diffraction patterns from (111), (002), and (022) planes of the rock-salt HEO. Nanoscale porosity between the columnar grains (outlined in red) was visible as bright contrast in the HRTEM images (Fig. 6c, d), indicative of lower material mass or thickness in the TEM specimen between the crystalline columnar grains. The top of the columnar grains showed a pyramidal shape (Fig. 6d), consistent with preferred adatoms addition at ascending steps on the top of columnar grains [30]. Interestingly, we found that there was an amorphous layer between the substrate and columnar grains (Fig. 6e). It is speculated that the amorphous layer results from the reaction between silicon and oxygen from the HEO after formation of columnar grains, as the [111] preferred orientation was likely from the lattice match between the substrate and target material at the very initial stage of the film growth: $d_{film\_}(111) = 2.45$ Å

and $d_{Si\_}(001) = 5.43$ Å, thus the lattice mismatch fraction is 0.55 (fraction $= (d_{Si} - d_{film})/d_{Si}$). The elemental distribution of a representative HEO film was measured with scanning transmission electron microscopy energy-dispersive X-ray spectroscopy (STEM-EDS), which showed that each element in the HEO is distributed uniformly through the thin film (Fig SI-4).

It was observed that energy fluence also affects the number of liquid droplets deposited on the thin film surface, which results from the ejection of melted target material by the laser [31, 32]. These droplets contain many atoms which do not separate to individual adatoms, and thereby form near spherical morphologies on the film surface or round patterns within the film. These droplets are known to influence film properties and are thus a key challenge of the PLD technique [33, 34]. The cross-section view of a droplet was observed by a STEM dark-field (STEM-DF) image (Fig. 6f) and showed the distinctive structure difference between the ejected droplets/fragments and surrounding columnar grains. In this image, the droplet impedes further growth of the columnar grains and degrades the uniformity of the thin film. However, from SEM imaging, it was observed that increasing the energy fluence produced fewer droplets on the HEO film surface (Fig. 7). An incorporation process of droplets/fragments into the surrounding columnar grains
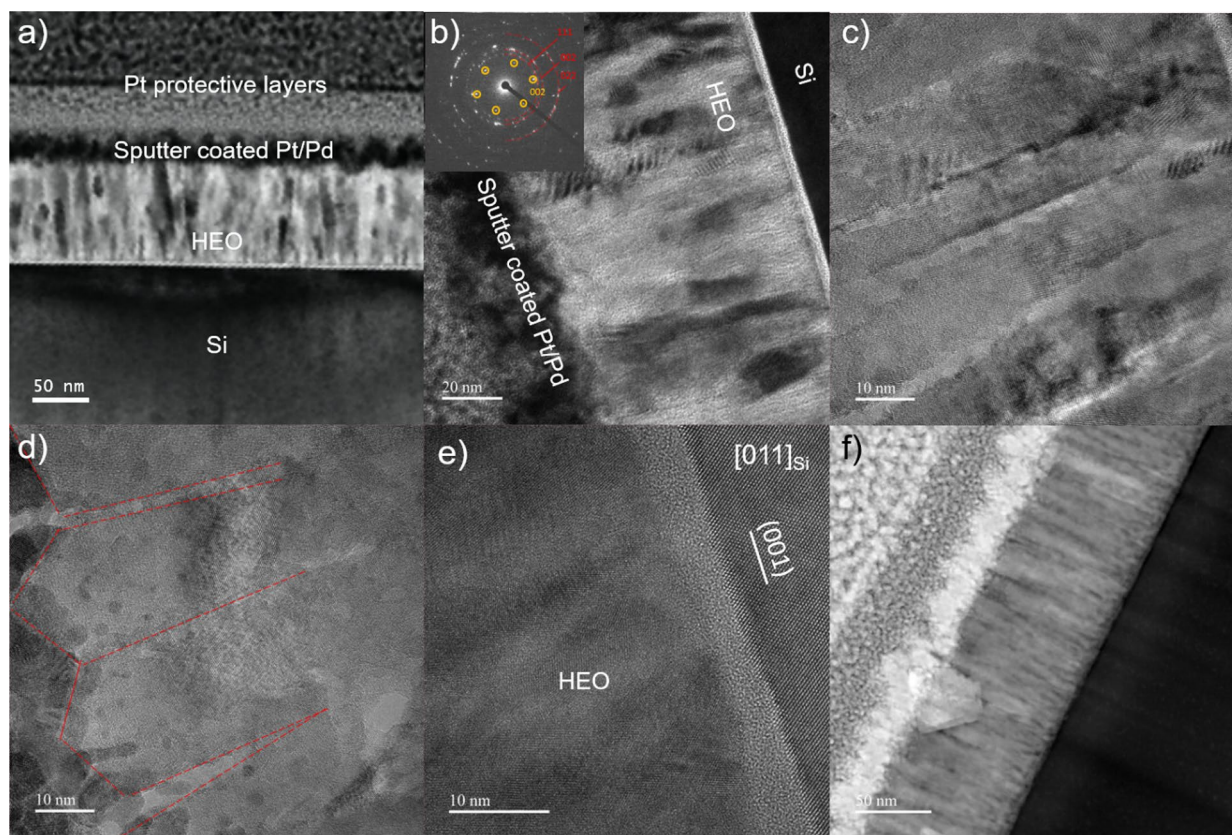
Figure 6: S/TEM images of cross-section view of the HEO film prepared at 5.3 J/cm^2. (a, b) BFTEM images of the HEO thin film deposited on a Si substrate. Inset in (b) is the corresponding SAED pattern. (c) HRTEM image showing the nanopores between columnar grains; (d) HRTEM image showing the pyramidal shape at the top of the HEO columnar grains; (e) HRTEM image at the interface between Si and HEO showing the presence of a thin amorphous layer. (f) STEM-DF image showing an ejected target droplet (or fragment) in the HEO thin film.

was observed on the HEO film surface (circled area in Fig. 7) at high energy fluence of 7.0 J/cm^2 and 8.1 J/cm^2. Additionally, at high energy fluence ablation predominates at the target surface so that there are fewer molten droplets produced and fewer droplets at the substrate surface.

Conclusion

In this work, a rock-salt HEO (Co$_{0.2}$Ni$_{0.2}$Cu$_{0.2}$Mg$_{0.2}$Zn$_{0.2}$)O) ceramic served as the target material for nanoporous thin film fabrication of a compositionally complex oxide by PLD which has great potential applications in batteries, catalysis, and sensors where high surface area, phase stability, compositional flexibility, and defect tolerance are desired. This work offers guidelines for single-phase thin film deposition of multicomponent oxides which otherwise would normally form secondary phases in the bulk when heat treated at elevated temperatures, such as the rock-salt HEO system used here. The fabricated thin films had the same crystal structure as targets and were compositionally uniform. The effect of energy fluence on film crystal structure and morphology was explored. Increasing energy fluence

increases crystallization of thin films even at low substrate temperature (300 °C in this work). The prepared HEO films have 3D island structures comprised of individual crystalline columnar grains and islands separated by connected random shaped nanopores, and the size of the columnar grains and islands (19 nm to 35 nm in average size) as well as pore size (9.3 to 20 nm in average size) increases with increasing energy fluence (3.4 to 7.0 J/cm^2). Increasing energy fluence enables adatoms to diffuse and crystalize to facilitate both deposition-driven impingement and surface-diffusion driven coalescence between columnar grains. Hence, energy fluence can be used to tune the size of islands and nanopores for customizing the design of electrodes, sensors, catalysts, etc. Increasing energy fluence also increases the film thickness, as more adatoms ablate from the target surface and arrive at the substrate. Additionally, increasing energy fluence reduces the number of droplets on the thin film surface, which is a major disadvantage of PLD. This work showed how modifying the kinetic energy of adatoms alters their diffusion in order to regulate nanoporosity. In addition to energy fluence, oxygen pressure and substrate temperature are also available for modification of kinetic energy. Moreover, increasing the energy barrier
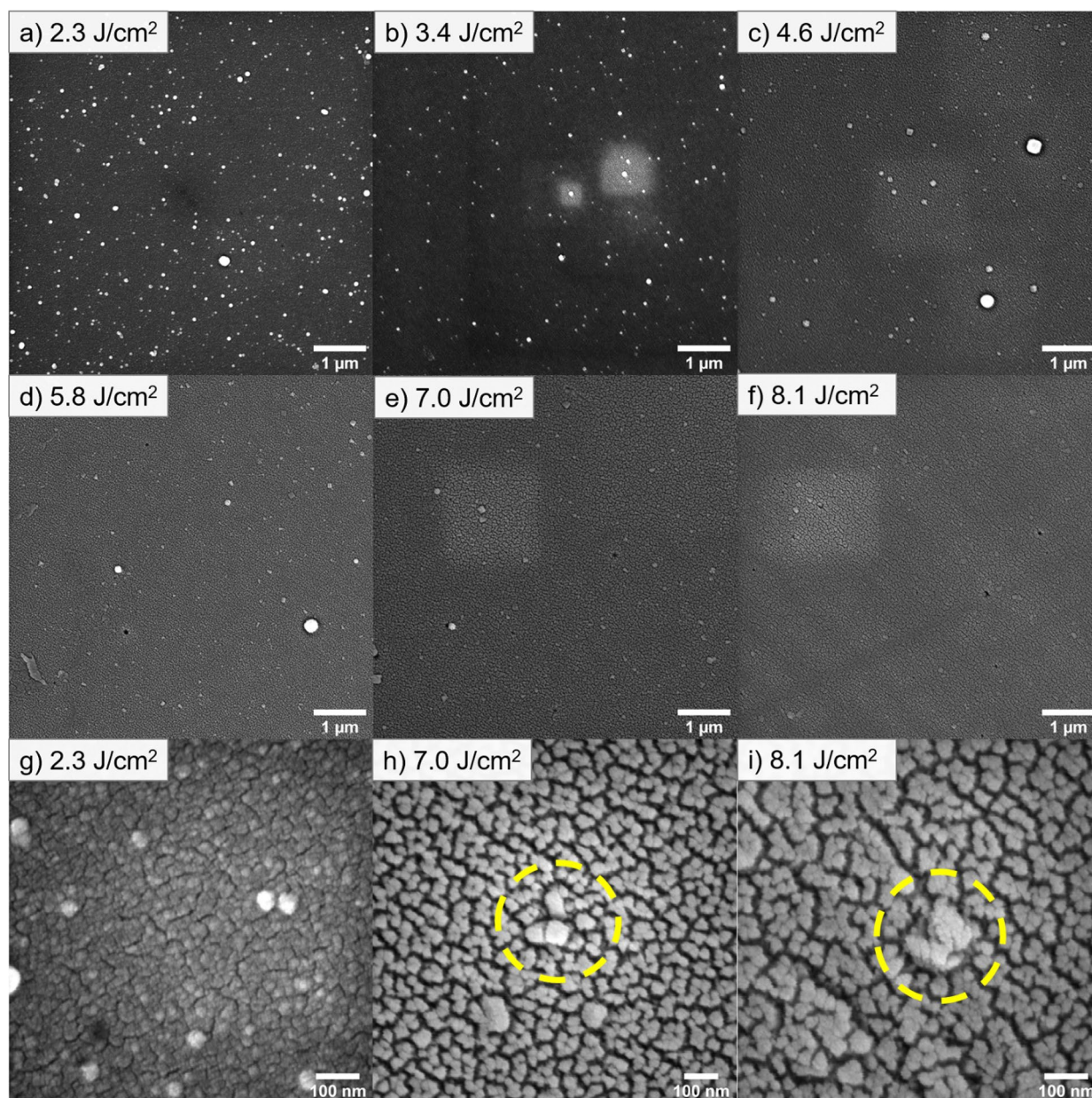
Figure 7: Droplet patterns on HEO thin film surface at different energy fluence: (a, g) 2.3 J/cm²; (b) 3.4 J/cm²; (c) 4.6 J/cm²; (d) 5.8 J/cm²; (e, h) 7.0 J/cm²; (f, i) 8.1 J/cm²; circled area shows decomposition of droplet patterns and their incorporation into surrounding columnar grains and islands.

for adatom diffusion is another strategy to introduce nanopores to PLD films. Building initial islands through surface etching or decoration and glancing angle deposition (GLAD) can effectively impede surface diffusion of adatoms.

Experimental methods

Target preparation

The bulk HEO target was prepared by reaction sintering of a blend of oxide nanopowders. Individual oxide nanopowders of CoO (50 nm reported particles size, 99.7 wt% purity), NiO (18 nm, 99.98%), CuO (25–55 nm, 99.95%), MgO (50 nm, 99.95%), and ZnO (18 nm, 99.95%) were sourced from US Research Nanomaterials Inc (Houston, TX, USA). Equimolar amounts of the five nanopowders were weighed out and mixed together using a mortar and pestle. The nanopowders were then blended and milled using a Fritsch Premium 7 (Fritsch GmbH, Idar-berstein, Germany) planetary ball mill at 300 rpm for 3 h. The nanopowders were suspended in isopropanol inside a Si_3N_4 jar and milled using Si_3N_4 milling media with a 10:1 ball to powder weight ratio and 20% volumetric ratio of milling media to the jar. After drying, the powders were poured
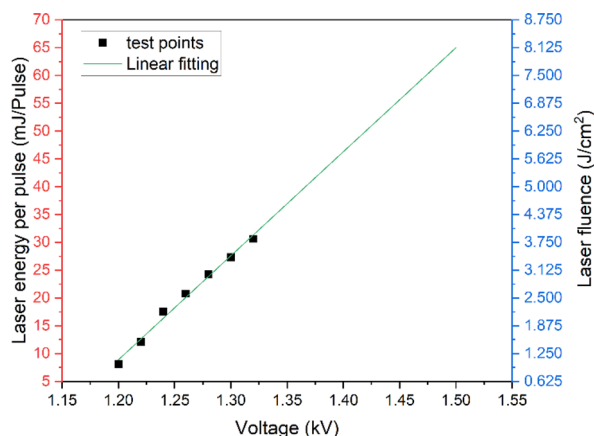
Figure 8: Laser energy and energy fluence change with voltage applied to the solid-state laser.

into a 20-mm-diameter graphite die and plunger set and cold pressed at 100 MPa for 10 min. Consolidation was performed using a Fuji model 825S (Fuji Electronic Industrial Co., Ltd., Kawasaki, Japan) spark plasma sintering (SPS) instrument at 900 °C for 10 min. A heating rate of 50 °C/min was used and an applied pressure of 30 MPa was used throughout the experiment. After consolidation, the HEO target was heat treated in air and quenched in order to insure a complete solid-state reaction and single-phase state. Heat treatment was performed using an elevator furnace (Model 1210BL, CM Furnaces, Bloomfield, NJ, USA) at 900 °C for 2 h. Quenching was achieved by lowering the sample and elevator into the path of a fan blowing room temperature air. The fabricated HEO target is dense with relative density as high as 99%.

HEO thin film preparation

Thin film preparation used a Nd:YAG solid laser with 266 nm wavelength and 10 ns pulse duration (Continuum SL III-10) and a high-vacuum deposition system (Neocera Pioneer 180 GLAD-PLD System). (001) Silicon with one-side polish (MTI Corporation) served as a substrate and was cleaned through ultrasonic treatment in acetone, isopropanol, and methanol for 5 min, respectively. The substrate–target distance (STD) was 57 mm and high purity O_2 (99.994%) served as the only inlet gas for pressure regulation during deposition. As an experiment variable, energy fluence changed via concentrating different laser energy on a spot with an area of 0.8 mm^2. The laser energy can be regulated by modifying voltage for laser excitation following a linear relation at relatively low energy period tested by an energy meter (Nova Ophir Photonics), as shown in Fig. 8. In this experiment, energy fluence increased from 1.1 to 8.1 J/cm^2

following a range of voltages from 1.20 to 1.50 kV to explore the effect of energy fluence on thin film structure. The deposition of rock-salt HEO (($Co_{0.2}Ni_{0.2}Cu_{0.2}Mg_{0.2}Zn_{0.2}$)O) thin films occurred at a total pressure of 50 mtorr and substrate temperature of 300 °C with 30,000 pulses at 10 Hz. After deposition, the prepared films were cooled down at 10 °C/min under the same pressure without post-annealing process.

Sample characterization

Crystal structure of both the HEO target and prepared thin films was characterized using a Rigaku SmartLab X-ray diffractometer with a Cu-Kα X-ray radiation under voltage of 40 kV and current of 44 mA. X-ray diffraction (XRD) pattern of the HEO target was collected at symmetric θ-2θ geometry under general Bragg–Brentano (BB) mode using parafocusing beam. XRD patterns of the deposited HEO films were obtained at θ-2θ geometry under general parallel beam/parallel slit analyzer (PB/PSA) mode. The top view and cross-section view of grains, columnar grains, and islands in the thin films as well as the thin film thickness and nanoporous morphology were observed through a TESCAN GAIA-3 XMH field-emission scanning electron microscope (FESEM) using an accelerating voltage of 7 kV under secondary-electron imaging mode. The working distance is around 5 mm during SEM observation. All the SEM samples were coated with 5 nm Pt/Pd to avoid charging using a Leica Sputter Coater 200. Thin film morphology with nanopores at high resolution, connection between the substrate and deposited films, localized crystal structure, film orientation, and compositional mapping were examined by a JEOL JEM-2800 Schottky field-emission scanning/transmission electron microscope (FE-S/TEM) attached with a Gatan Oneview IS camera for imaging, an ASTAR® /precession electron diffraction (PED) system (NanoMEGAS, Belgium), and dual dry solid-state 100 mm^2 energy-dispersive X-ray spectroscopy (EDS) detectors. High-resolution TEM (HRTEM), bright-field TEM (BFTEM) and STEM dark-field (STEM-DF) images, selected area electron diffraction (SAED) patterns, PED analysis, and EDS spectra were acquired at an accelerating voltage of 200 kV. A small scanning step size of 2 nm was used in PED for orientation mapping. The TEM cross-sectional sample of the HEO film was fabricated by focused ion beam (FIB) cutting in a FEI Quanta 3D FEG dual-beam FIB-SEM. Changes of plasma plume were recorded and tracked by digital photos taken with a Canon EOS 2000D. The size of columnar grains and islands were described with their Feret diameter, which refers to the largest distance separating two points along boundaries in a selected area.

Acknowledgments

Author contributions

HG and WJB conceived of the study. HG tested the laser energy, fabricated the HEO thin films, and performed XRD and SEM characterization. ADD prepared the HEO target. XW performed TEM experiments. HG wrote most of the paper. All co-authors contributed to the final version. WJB supervised the study.

Data availability

The datasets generated during and/or analyzed during the current study are available from the corresponding author on reasonable request.

Declarations

Conflict of interest No competing interests.

Open Access

Supplementary Information

The online version contains supplementary material available at https://doi.org/10.1557/s43578-021-00473-2.

References

1. C.M. Rost, E. Sachet, T. Borman, A. Moballegh, E.C. Dickey, D. Hou, J.L. Jones, S. Curtarolo, J.-P. Maria, Entropy-stabilized oxides. Nat. Commun. **6**(1), 8485 (2015)

2. A. Gautam, M.I. Ahmad, Low-temperature synthesis of five component single phase high entropy oxide. Ceram. Int. (2021). https://doi.org/10.1016/j.ceramint.2021.04.128

3. D. Berardan, A.K. Meena, S. Franger, C. Herrero, N. Dragoe, Controlled Jahn-Teller distortion in (MgCoNiCuZn)O-based high entropy oxides. J. Alloys Compds. **704**, 693 (2017)

4. G.N. Kotsonis, P.B. Meisenheimer, L. Miao, J. Roth, B. Wang, P. Shafer, R. Engel-Herbert, N. Alem, J.T. Heron, C.M. Rost, J.-P. Maria, Property and cation valence engineering in entropy-stabilized oxide thin films. Phys. Rev. Mater. **4**(10), 100401 (2020)

5. A. Amiri, R. Shahbazian-Yassar, Recent progress of high-entropy materials for energy storage and conversion. J. Mater. Chem. A **9**(2), 782 (2021)

6. M. Lorenz, M.S. Ramachandra Rao, 25 years of pulsed laser deposition. J. Phys. D: Appl. Phys. **47**(3), 030301 (2013)

7. P. Kuppusami, V.S. Raghunathan, Status of pulsed laser deposition: challenges and opportunities. Surf. Eng. **22**(2), 81 (2006)

8. M. Xu, J. Yu, Y. Song, R. Ran, W. Wang, Z. Shao, Advances in ceramic thin films fabricated by pulsed laser deposition for intermediate-temperature solid oxide fuel cells. Energy Fuels **34**(9), 10568 (2020)

9. L. Indrizzi, N. Ohannessian, D. Pergolesi, T. Lippert, E. Gilardi, Pulsed laser deposition as a tool for the development of all solid-state microbatteries. Helvetica Chim. Acta. **104**(2), e2000203 (2021)

10. J. Wang, J. Yang, A.K. Opitz, W. Bowman, R. Bliem, G. Dimitrakopoulos, A. Nenning, I. Waluyo, A. Hunt, J.-J. Gallet, B. Yildiz, Tuning point defects by elastic strain modulates nanoparticle exsolution on perovskite oxides. Chem. Mater. **33**(13), 5021 (2021)

11. H.M. Christen, G. Eres, Recent advances in pulsed-laser deposition of complex oxides. J. Phys. Condens. Matter. **20**(26), 264005 (2008)

12. J.S. Horwitz, *Pulsed-Laser Deposition, in Surface Engineering* (ASM International, Materials Park, 1994)

13. P.R. Willmott, J.R. Huber, Pulsed laser vaporization and deposition. Rev. Mod. Phys. **72**(1), 315 (2000)

14. A.D. Dupuy, X. Wang, J.M. Schoenung, Entropic phase transformation in nanocrystalline high entropy oxides. Mater. Res. Lett. **7**(2), 60 (2019)

15. V. Jacobson, D. Diercks, B. To, A. Zakutayev, G. Brennecka, Thin film growth effects on electrical conductivity in entropy stabilized oxides. J. Eur. Ceram. Soc. **41**(4), 2617 (2021)

16. M.J. Aziz, Film growth mechanisms in pulsed laser deposition. Appl. Phys. A. **93**(3), 579 (2008)

17. V.L. Tassev, S.R. Vangala, Thick hydride vapor phase heteroepitaxy: a novel approach to growth of nonlinear optical materials. Crystals **9**(8), 393 (2019)

18. V.I. Trofimov, V.G. Mokerov, Epitaxial growth kinetics in the presence of an Ehrlich-Schwoebel barrier: comparative analysis of different models. Mater. Sci. Eng. B **89**(1), 420 (2002)

19. F. Otto, P. Penzler, T. Rump, Discretisation and numerical tests of a diffuse-interface model with ehrlich-schwoebel barrier, in *Multiscale Modeling in Epitaxial Growth*. ed. by A. Voigt (Birkhäuser, Basel, 2005), p. 127

20. M. Załuska-Kotur, H. Popova, V. Tonchev, Step bunches, nanowires and other vicinal "Creatures"—Ehrlich–Schwoebel effect by cellular automata. Crystals **11**(9), 1135 (2021)

21. S. Shin, H.S. Han, J.S. Kim, I.J. Park, M.H. Lee, K.S. Hong, I.S. Cho, A tree-like nanoporous WO_3 photoanode with enhanced charge transport efficiency for photoelectrochemical water oxidation. J. Mater. Chem. A **3**(24), 12920 (2015)

22. G. Atanasova, A.O. Dikovska, T. Dilova, B. Georgieva, G.V. Avdeev, P. Stefanov, N.N. Nedyalkov, Metal-oxide nanostructures produced by PLD in open air for gas sensor applications. Appl. Surf. Sci. **470**, 861 (2019)

23. A. Infortuna, A.S. Harvey, U.P. Muecke, L.J. Gauckler, Nanoporous $Ni–Ce_{0.8}Gd_{0.2}O_{1.9−x}$ thin film cermet SOFC anodes prepared by pulsed laser deposition. Phys. Chem. Chem. Phys. **11**(19), 3663 (2009)

24. R. Eason, *Pulsed Laser Deposition of Thin Films: Applications-Led Growth of Functional Materials* (Wiley, Hoboken, 2007)

25. R. Boidin, T. Halenkovič, V. Nazabal, L. Beneš, P. Němec, Pulsed laser deposited alumina thin films. Ceram. Int. **42**(1 Part B), 1177 (2016)

26. D.H.A. Blank, M. Dekkers, G. Rijnders, Pulsed laser deposition in Twente: from research tool towards industrial deposition. J. Phys. D Appl. Phys. **47**(3), 034006 (2013)

27. G. Beck, H. Fischer, E. Mutoro, V. Srot, K. Petrikowski, E. Tchernychova, M. Wuttig, M. Rühle, B. Luerßen, J. Janek, Epitaxial Pt(111) thin film electrodes on YSZ(111) and YSZ(100): preparation and characterization. Solid State Ion. **178**(5), 327 (2007)

28. G. Jeffers, M.A. Dubson, P.M. Duxbury, Island-to-percolation transition during growth of metal films. J. Appl. Phys. **75**(10), 5016 (1994)

29. J.M. Warrender, M.J. Aziz, Evolution of Ag nanocrystal films grown by pulsed laser deposition. Appl Phys. A **79**(4), 713 (2004)

30. S.C. Wang, G. Ehrlich, Adatom motion to lattice steps: a direct view. Phys. Rev. Lett. **70**(1), 41 (1993)

31. T. García, E. de Posada, L. Ponce, J.L. Sánchez, S. Díaz, E. Pedrero, F. Fernández, P. Bartolo-Pérez, J.L. Peña, R. Diamant, J.A.M. Pereira: Textured strontium ferrite thin films grown by PLD. Mater. Lett. **49**(5), 294 (2001)

32. L.A. Michel, L. Laetitia and I. Tatiana: Experimental and theoretical study of dual-crossed-beam pulsed laser deposition, in *Proc.SPIE*, vol. 4070 (City, 2000)

33. W. Liu, J.-P. Wan, W.-P. Cai, J.-H. Liang, X.-S. Zhou, X.-G. Long, Characterization of zirconium thin films deposited by pulsed laser deposition. Chin. Phys. B **23**(9), 098103 (2014)

34. T. Yoshitake, G. Shiraishi, K. Nagayama, Droplet-free thin films prepared by pulsed laser deposition using a vane velocity filter. Jpn. J. Appl. Phys. **41**(1 Part 1, No, 2A), 836 (2002)